



HAL
open science

Density fluctuation analysis very near above and below critical point using morphological and spatiotemporal information

Ana Oprisan, Sorinel Oprisan, Yves Garrabos, Carole Lecoutre-Chabot,
Daniel Beysens

► To cite this version:

Ana Oprisan, Sorinel Oprisan, Yves Garrabos, Carole Lecoutre-Chabot, Daniel Beysens. Density fluctuation analysis very near above and below critical point using morphological and spatiotemporal information. *The European Physical Journal Plus*, 2021, 136 (5), 523 (17 p.). 10.1140/epjp/s13360-021-01531-8. hal-03230780

HAL Id: hal-03230780


<https://hal.science/hal-03230780v1>

Submitted on 21 May 2021

HAL is a multi-disciplinary open access archive for the deposit and dissemination of scientific research documents, whether they are published or not. The documents may come from teaching and research institutions in France or abroad, or from public or private research centers.

L'archive ouverte pluridisciplinaire **HAL**, est destinée au dépôt et à la diffusion de documents scientifiques de niveau recherche, publiés ou non, émanant des établissements d'enseignement et de recherche français ou étrangers, des laboratoires publics ou privés.

1 **Density fluctuation analysis very near above and below**
 2 **critical point using morphological and spatiotemporal**
 3 **information**

4 Ana Oprisan^{1,a} , Sorinel A. Oprisan¹, Yves Garrabos², Carole Lecoutre-Chabot²,
 5 Daniel Beysens³

6 ¹ Department of Physics and Astronomy, College of Charleston, 66 George Street, Charleston, SC 29424,
 7 USA

8 ² CNRS, Université de Bordeaux, Bordeaux INP, ICMCB, UMR 5026, F-33600 Pessac, France

9 ³ Physique et Mécanique des Milieux Hétérogènes, CNRS, ESPCI, PSL Research University, Sorbonne
 10 Université, Sorbonne Paris Cité, Paris, France

11 Received: 8 March 2021 / Accepted: 4 May 2021

14 **Abstract** We investigate the fractal nature of critical fluctuations in sulfur hexafluoride
 15 (SF₆) under microgravity conditions. For this purpose, we use the Bidimensional Empiric
 16 Mode Decomposition (BEMD) approach to separate the spatial scales of fluctuations in
 17 orthogonal Independent Mode Functions (IMFs). Statistical analysis of three morphology
 18 measures (area, eccentricity, and orientation of convex objects in recorded images) across
 19 different IMFs shows that critical fluctuations obey power-laws across multiple spatial scales.
 20 We also perform a spatiotemporal analysis of fluctuations by extracting one line of pixels
 21 from each image and creating a temporal stack from successive images, or “waterfalls.”
 22 The spatiotemporal section analysis along the spatial direction reveals multiple spatial scales
 23 present in the original fluctuating image. The analysis of the “waterfalls” along the temporal
 24 direction identifies a common power-law temporal behavior across all spatial scales. Our
 25 results show that critical fluctuations very near critical temperature (T_c) have a fractal structure
 26 captured by power-laws with multiple critical exponents. The morphology analysis shows
 27 that very near T_c , the fluctuating domains are mostly spherical with some anisotropy.

28 **1 Introduction**

29 Many experiments on the critical behavior of gas-liquid and binary fluids systems have been
 30 performed, and they go back to over a hundred years [5, 7, 9, 25, 26]. Many of them are light
 31 scattering-based experiments [6, 35, 53, 79] that determine thermophysical parameters close
 32 to the critical point by relying almost exclusively on Fourier analysis [14, 32, 58, 59]. Fourier
 33 transform is a convenient method of switching back and forth between the real physical space
 34 (x, y) of the light scattering in the recorded image and the corresponding conjugated space of
 35 wavenumbers ($k_x = 2\pi/x, k_y = 2\pi/y$). Compared to the Fourier method, there are only a
 36 few studies on direct observation of the scattered light intensity fluctuations in physical space

^a e-mail: oprisana@cofc.edu (corresponding author)

(x, y) of the recorded images [10,23,35,38,39]. Asher and Pankow [2] performed a somewhat similar direct observation of light intensity fluctuations, although they used a laser-induced fluorescence method to measure the timescales of surface concentration fluctuations.

In real space recorded images, light intensity fluctuations appear as domains whose intensity is different from the image's mean intensity. In equilibrium conditions, these fluctuations have large enough sizes to become detectable with optical cameras only when the system is close to criticality. On the other side, non-equilibrium fluctuations become giant thanks to the coupling of spontaneous fluctuations with the existing gradient [77]. This is increasingly true if one removes gravity [75]. The direct imaging of critical fluctuations may answer fundamental questions regarding the correlation between thermal fluctuations and critical percolation points [18,70]. This connection rests on a precise criterion to define clusters that emerge from fluctuations during phase separation, and this up to now is still lacking.

The fluctuations of light intensity $\delta i(x, y)$ detected by light scattering experiments are determined by the corresponding order parameter fluctuations. In pure fluids near their critical point, the order parameter is the reduced critical density, $M = \rho/\rho_c - 1$, where $\rho(\rho_c)$ is the (critical) density of the system.

The signature of self-similarity of the fluctuating domains is the existence of a power-law dependence between the number of the convex areas and their "mass," i.e., the number of pixels in the image belonging to a convex domain [24]. Mathematically, the existence of a scaling equation for an observable $A(r)$, which is a function of a variable r , establishes the quantitative connection between the power-laws and fractals:

$$A(\lambda r) = \lambda^n A(r), \quad (1)$$

where λ is a constant factor and n is a scaling exponent, independent of r [48]. Indeed, a power-law such as $y(r) = \alpha r^n$ is among the functions that obey the above scaling law since $y(\lambda r) = \alpha(\lambda r)^n = \lambda^n y(r)$. The above scaling equation is identical to the recursion formula of the renormalization group theory when recursively integrating the short distance degrees of freedom of the system to generate a sequence of effective Hamiltonians corresponding to increasing scale [47,74,80,81]. The physical quantity $A(r)$ may not be extensive at the critical point due to the long-range correlation of critical fluctuations. As the system approaches a critical point, the asymptotic behavior of the physical quantity $A(r)$ as the length scale changes $L \rightarrow L' = L/r$ usually gives a power-law [29,30,73]:

$$A(L') = A(L/r) \propto r^{-\phi} A(L). \quad (2)$$

Near the critical points of phase transition, a new order driven by strong and long-range correlations between dynamic events emerges at all the system's spatial scales. Such a (re)organization of the system occurs at all spatial scales and can be best captured mathematically by power-laws and fractal dimensions [69]. A fluid near its critical point is in constant contact with a thermostat with which it exchanges energy that leads to a coherent macroscopic behavior [17]. Such a process mediated by long-range correlations among fluctuating domains reflects the unity of the physical laws spanning multiple spatiotemporal scales and is captured by scale-free power-law distributions of observables.

The first study that identified an experimental power-law was done by Vilfredo Pareto and modeled the distribution of individuals' incomes, which is called nowadays Pareto law [63]. He found that the relative number of individuals with an annual income larger than a specific value x was proportional to the power of x . Since then, fractal structures characterized by power-law distributions were discovered in the turbulent flow [71], earthquake dynamics

83 occurrence of an infinite cluster can be associated with the divergence of the fluctuations near
84 the critical point [36].

85 Our main result is that critical fluctuations very near critical temperature (T_c) have a fractal
86 structure captured by power-laws with multiple critical exponents. Our current approach's
87 advantages are that (1) data analysis is performed in the spatial domain without using Fourier
88 transforms, (2) the image analysis is data-driven, i.e., all measures related to spatiotemporal
89 behavior of the fluctuations are directly related to observed intensity fluctuations, and (3) the
90 BEMD-based analysis is valid even for nonlinear and non-stationary processes.

91 2 Experimental setup

92 Images of large thermal fluctuations near the critical point ($T_c = 318.733$ K, $P_c = 37.586$ bar,
93 $\rho_c = 5.0581$ mol l⁻¹) of sulfur hexafluoride (SF₆) in microgravity conditions were recorded
94 using ALICE 2 instruments onboard of 1999 MIR space station [15,28,49,51,55]. In this
95 microgravity experiment, SF₆ above its critical temperature T_c was quenched by quickly
96 decreasing its temperature with steps of 300 μ K. Several sets of thermal quenches (see Fig.
97 1 in [56]) were performed from the one-phase region above critical temperature into the
98 two-phase region below T_c that resulted in phase separation [55,56]. The temperature was
99 monitored with three thermistors placed inside the SCU. For image analysis, we cropped the
100 most extensive possible rectangular area without including data markers. In this paper, we
101 only discuss image processing results based on the last 300 μ K thermal quench that stepped
102 through the critical temperature [39,56,60]. The system was prepared at the critical density
103 with the order parameter $M = (\rho - \rho_c)/\rho = 0.0 \pm 0.02\%$. The 300 μ K temperature quench
104 through T_c started the phase separation of the fluid (see [39,56,60] for a detailed description
105 of the experimental procedure). Since the phase separation has begun during the last 300 μ K
106 thermal quench, we concluded that T_c was somewhere between the upper (UP, i.e., $T > T_c$)
107 and lower (DOWN, i.e., $T < T_c$) plateaus. The exact location of T_c measured from the
108 DOWN plateau was determined with the histogram method to be $46.74 \pm 0.03 \mu$ K [55] and
109 in the range of 15 μ K to 42 μ K using Dynamic Differential Microscopy (DDM) [56].

110 The density fluctuations were visualized through light transmission normal to the sapphire
111 windows using a He-Ne laser with 632.8 nm wavelength and about 100 μ W maximum power
112 (see also [60] for a detailed description). Laser stability after 1 h was estimated to be better
113 than 0.3 %. An optical microscope of 3.1 μ m resolution was also used to record a small SCU
114 region. We used 166 images (6.64s) recorded for UP ($T > T_c$) plateau. While the first 71
115 images of the 166 UP series were recorded with the microscope focused on the sapphire
116 window, the rest were recorded with the focal plane at the cell's center. For the DOWN
117 ($T < T_c$) plateau, we used 479 images (19.16s). All images for the DOWN region were
118 recorded with the focal plane at the center of the cell. The full description of the experiment
119 is presented elsewhere [55,56,60].

120 3 Methods

121 3.1 Bidimensional Empiric Mode Decomposition (BEMD)

122 We use a new data-driven method for multi-scale analysis of critical fluctuations. The method
123 naturally separates the spatial scales based on the image content. The BEMD method breaks
124 the original image into different orthogonal spatial scales called Intrinsic Mode Function

125 (IMF) and one residual quantity [60]. We probe the fractal nature of critical fluctuations by
126 separating spatial scales with the BEMD method followed by (1) morphological analysis and
127 (2) spatiotemporal cross sections (“waterfalls”) of all IMFs. For this purpose, the BEMD
128 first separates the fluctuations in orthogonal spatial scales that contrast the morphology and
129 spatial properties more intuitively. We hypothesize that if critical fluctuations have a fractal
130 structure, then morphology measures and spatiotemporal structures should observe similar
131 evolutions across all spatial scales represented by individual IMFs.

132 In the past, the Empirical Mode Decomposition (EMD) has been applied to earthquake
133 analysis [41,64], structural diagnosis [31,52], characterization of non-stationary biological
134 processes [44], mechanical fault diagnosis [84,85], and ocean waves analysis [72]. One
135 advantage of EMD over traditional spectral analysis methods is that it can be applied even to
136 nonlinear and non-stationary signals and produces linear and stationary IMFs [43]. Intuitively,
137 the EMD is a data-driven adaptive method that allows recursive removal of oscillations (IMFs)
138 by repeated subtraction of an appropriately defined baseline [34,40–44]. For two-dimensional
139 data sets (images), we used a BEMD algorithm [65] that requires no pre-determined filter or
140 wavelet function [68]. The BEMD has been applied to texture extraction and image filtering
141 [45], finding the gold mineral deposition [40], the discovery of tin-copper polymetallic ore
142 field [16] by gravity anomalies captured by satellite images, image denoising [4,50], content-
143 based image retrieval [1], and fusion of multispectral and remote sensing [27,34,37]. We
144 recently expanded the application of the BEMD method and combined it with the Dynamic
145 Differential Microscopy (DDM) to the analyses of critical fluctuations [60]. All the details
146 of decomposing fluctuation images based on BEMD are described in [60]. BEMD is a fully
147 adaptive multi-scale decomposition because it operates on the local extremum sequence. The
148 decomposition is carried out by direct extraction of the local energy associated with the signal
149 itself’s intrinsic time-scales. This approach is different from the wavelet-based multi-scale
150 analysis that characterizes the scale of a signal event using pre-specified basis functions [82].

151 For this study, we only considered three IMFs, plus the residual image [60]. Representative
152 examples of the original images, their first three IMFs, and the residual are shown in Fig. 1.
153 The BEMD decomposition contains the fluctuations from finest to coarsest spatial scale.
154 Since the sifting process extracts from the original image (Fig. 1A1 and A2) first the highest
155 spatial frequency (Fig. 1B1 and B2), the first IMF mode corresponds to the short-range
156 fluctuations, which we expect to dominate very close to the critical point. Conversely, the
157 image tendency and the long-range correlations of fluctuations are contained in the next two
158 modes (Fig. 1C1-C2 and D1-D2). The residue (Fig. 1E1 and E2) represents the largest spatial
159 scale of fluctuations obtained from the data. The residual is usually used as a background
160 image to correct for nonuniform illumination.

161 3.2 Spatiotemporal cross sections

162 The spatiotemporal correlations of fluctuations could be captured with the stacked one-
163 dimensional sections through individual images, i.e., “waterfalls” [39]. For this purpose, a
164 horizontal line of pixels was extracted from successive images at the same location, which
165 gave the spatial dimension of the image, called “space” in Fig. 2A1. The rows of pixels (one
166 row from each recorded image) were stacked according to the image index (time) along the
167 vertical direction, which gave the temporal dimension called “time” in (see Fig. 2)A1.

168 To obtain the original spatiotemporal (“waterfall”) images, we first applied the BEMD
169 decomposition to the original images, as shown in Fig. 1. Subsequently, we created for each
170 IMF order the corresponding spatiotemporal (“waterfall”) image as described above and
171 shown in Fig. 2A1-A4. An optimum gray-level threshold was selected for each line of pixels,

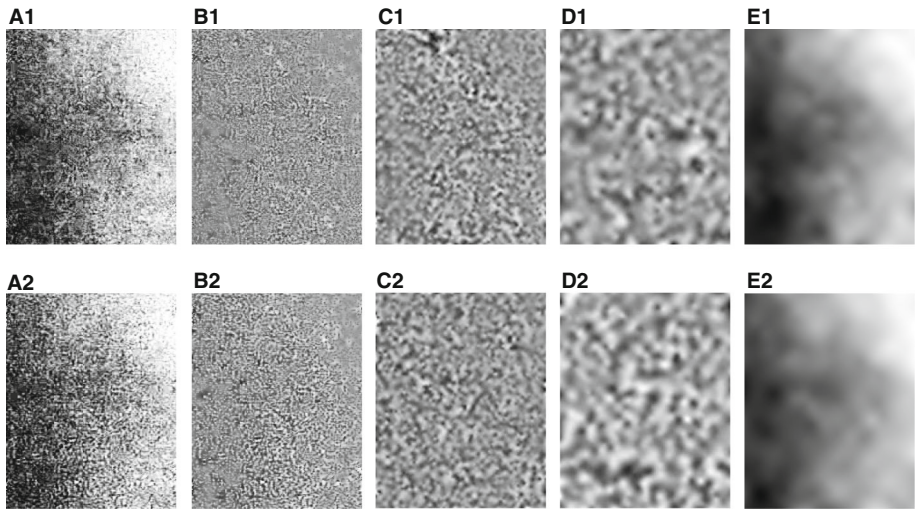


Fig. 1 The original images (A1 above T_c (UP with cell centered focus) and A2 below T_c (DOWN with cell centered focus)), the first three IMFs (B1-D1 for UP and B2-D2 for DOWN), and the residual image (E1 for UP and E2 for DOWN) for the image index 100 of UP and the image index 200 of DOWN region. Above critical temperature (panels A1-E1), the finest spatial scale (B1) shows small size fluctuations, which correspond to the fluctuations' finest spatial scale. For the DOWN region (B2), the first IMF's characteristic spatial distance seems to be comparable to UP, which is consistent with the early stage phase separation processes. The coarse spatial scales (C and D) show long-range correlation patterns of fluctuations. The residue (E) has a structure that suggests a long-range correlation of fluctuations

172 and the “waterfalls” were converted to black and white images (see Fig. 2B1-B4). We chose
 173 one threshold per line instead of a single threshold for the entire “waterfall” image because
 174 each line belongs to a different fluctuation image. This way, each line of pixels is thresholded
 175 based on the correct context it belongs to, i.e., its original image. To binarize the original
 176 grayscale images, we computed for each image a threshold based on Otsu's method [62].
 177 Otsu's method chooses a threshold that minimizes the intraclass variance of the thresholded
 178 black and white pixels. Although we only show in Fig. 2 the stack of rows through the middle
 179 of each image, we repeated the same procedure at 25 % and 75 % of image height and found
 180 no statistical difference with the results presented here for the central line of pixels. A similar
 181 approach was used for the DOWN region. The black and white thresholded grayscale images
 182 were used for edge detection of convex objects during morphology analysis.

183 4 Results

184 4.1 Morphological analysis of critical fluctuations

185 We used an in-house Matlab code to compute a set of properties specified by the 8-connected
 186 component (object) in the binarized fluctuation images (see Fig. 3B). In a two-dimensional
 187 image on a rectangular lattice, any given pixel is connected with eight adjacent pixels if their
 188 edges or corners touch, as shown in Fig. 3A. Two adjoining pixels are part of the same object
 189 if they are both on and are connected along the horizontal, vertical, or diagonal direction
 190 (see Fig. 3A for an 8-connected central pixel). Out of the 25 different properties computed,

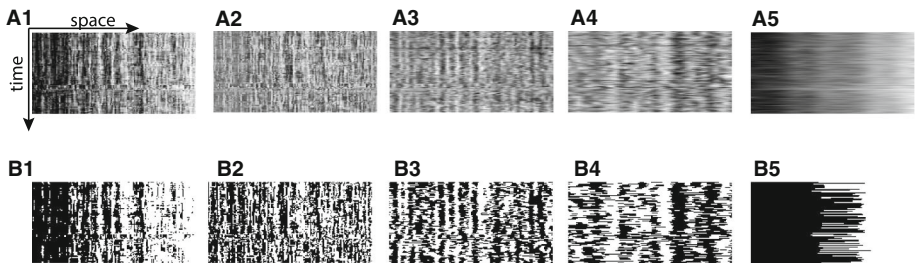


Fig. 2 Stacks of one-dimensional sections through the center of each fluctuation image of the UP region. The original (A1) grayscale images were separated into three IMFs plus a residual image using the BEMD algorithm (A2-A5). The shortest spatial scale is contained in A2 and the longest in A5. The corresponding thresholded black and white images (B1-B5) allow a clear identification of the boundaries of convex domains (black pixels)

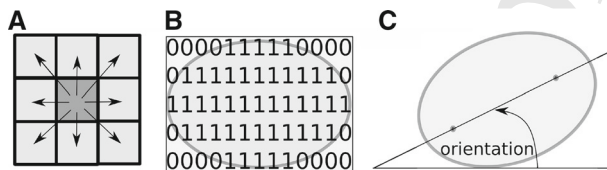


Fig. 3 (A) In two-dimensional images, an 8-connected central pixel has similar pixels along edges or corners. Two adjoining pixels are part of the same object if they are both on and are connected along the horizontal, vertical, or diagonal direction. (B) The eccentricity of a morphological object is the ratio of the distance between the foci of the ellipse and its major axis length. The value is between 0 (circle) and 1 (line segment). (C) The orientation of an elliptical object is given by the angle between the x-axis and the major axis of the ellipse. The value is in degrees, ranging from -90° to 90° . The two dots on the major axis represent the foci of the ellipse

191 we only present the statistics of the three most relevant measures for the morphology of
 192 fluctuations, i.e., area, eccentricity (see Fig. 3B), and orientation (see Fig. 3C).

193 At least 40% of the compact, i.e., convex, objects with clear boundaries have an area
 194 of one arbitrary unit (see Fig. 4A1-B1 for the original image, A2-B2 for IMF1, and A3-
 195 B3 for IMF2). As expected, large objects are scarce, reflected by a power-law decay of
 196 the percentage of compact objects' area versus their size (see Fig. 4A1-B1 for the original
 197 images). The statistics of only three representative images are shown in Fig. 4A1-A3 and
 198 B1-B3, respectively. The slope of the log-log plots shown in Fig. 4 represents the power-
 199 law exponents. The UP region has the first 71 images recorded with the focal plane of the
 200 microscope on the sapphire window of the SCU and the rest with the focal plane at the center
 201 of the SCU. The statistical analysis was performed separately for the two subsets of images
 202 recorded above T_c . Our statistical analysis of the morphology of fluctuation using convex
 203 area measure revealed no statistically significant difference between the 71 images and the
 204 rest for the UP region (see Fig. 4). As a result, the subsequent statistical analysis for other
 205 morphological measures (eccentricity and orientation) lumped together the two subsets of
 206 the UP dataset. From the UP region images recorded with the focal plane at the center of the
 207 SCU (Fig. 4A1-A3) and from the DOWN region (Fig. 4B1-B3), we only show the log-log
 208 plots for a set of three images selected at the beginning of the set, in the middle, and at the
 209 end of the respective dataset.

210 We fitted all area distributions for every image with power-laws given by $\%objects \propto$
 211 $area^n$, where the exponent values n are shown in Fig. 5A1-A2 for all images and their IMFs.

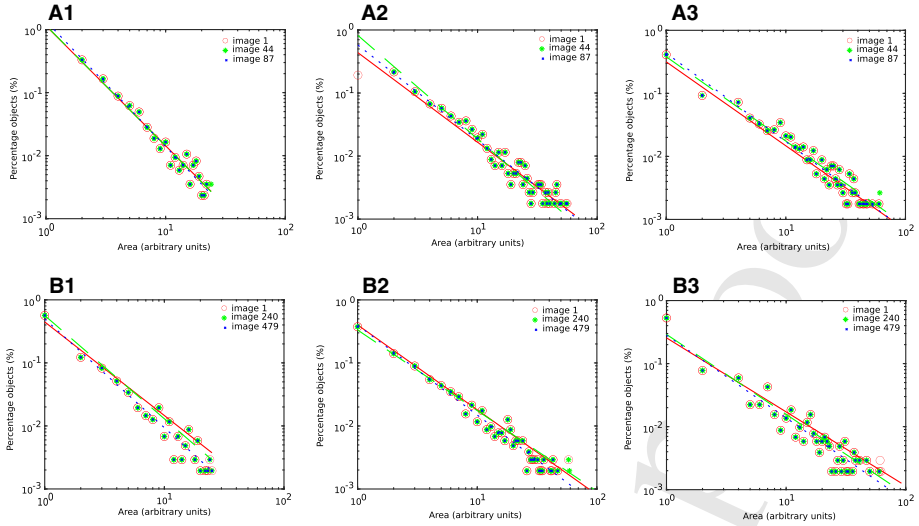


Fig. 4 The distribution of the area of the convex objects identified in fluctuations images. The top panels are for the original images (A1) and the first two IMFs (A2 and A3) of the UP region ($T > T_c$) with the focal plane in the center of the SCU. The bottom panels (B1-B3) correspond to the DOWN region ($T < T_c$) with the focal plane in the center of the SCU. The panels A1-B1 represent the original images, the panels A2-B2 represent the first IMF, and A3-B3 correspond to the second IMF. For each region UP/DOWN, we selected only three images

212 The area distributions of the third and fourth IMF are not shown, but a numerical summary
 213 is presented in Table 1. A summary of the UP plateau's power-law exponents is shown in
 214 Fig. 5A1, where the window- and center-focused data are separated by a vertical dashed line.
 215 Although we monitored multiple measures of the goodness of fit, e.g., the sum of squared
 216 error, the root mean square error, we only show in Fig. 5B1-B2 the adjusted R^2 coefficient
 217 as a measure of the goodness of fit. Adjusted $R^2 \in [-1, +1]$ determines the extent of the
 218 dependent variable's variance, which the independent variable can explain. The higher the
 219 adjusted R^2 , the better the regression equation captures the dependent variable's variance by
 220 the chosen independent variable(s). The average adjusted R^2 coefficient was over 92 % for
 221 the original images and the first IMF and over 87 % for IMF2. From Fig. 5A1, we notice a
 222 significant variance of the power-law exponent for the first 71 images of the UP plateau than
 223 the rest of the recording. Since the mean values across all original and IMFs are consistent
 224 and statistically identical both for the first 71 images recorded with the window focus and the
 225 rest of the images of the UP plateau recorded with the focus plane at the center of the SCU,
 226 the observed larger variance for the first subset is not due to the location of the focal plane.
 227 A possible explanation for the observed variability is that the first 71 images are recorded
 228 closer to when the thermal quench was applied and related to transient phenomena during
 229 thermal equilibration. An alternative explanation could reside in the fact that the proximity
 230 to the cell border alters the critical fluctuations due to the presence of preferential adsorption
 231 on lengthscale ξ (see [8, 83] and references therein).

232 The vertical dashed line in Fig. 5A1 separates the first 71 images of the UP dataset recorded
 233 with the focal plane on the sapphire window from the images recorded with the focal plane
 234 at SCU center.

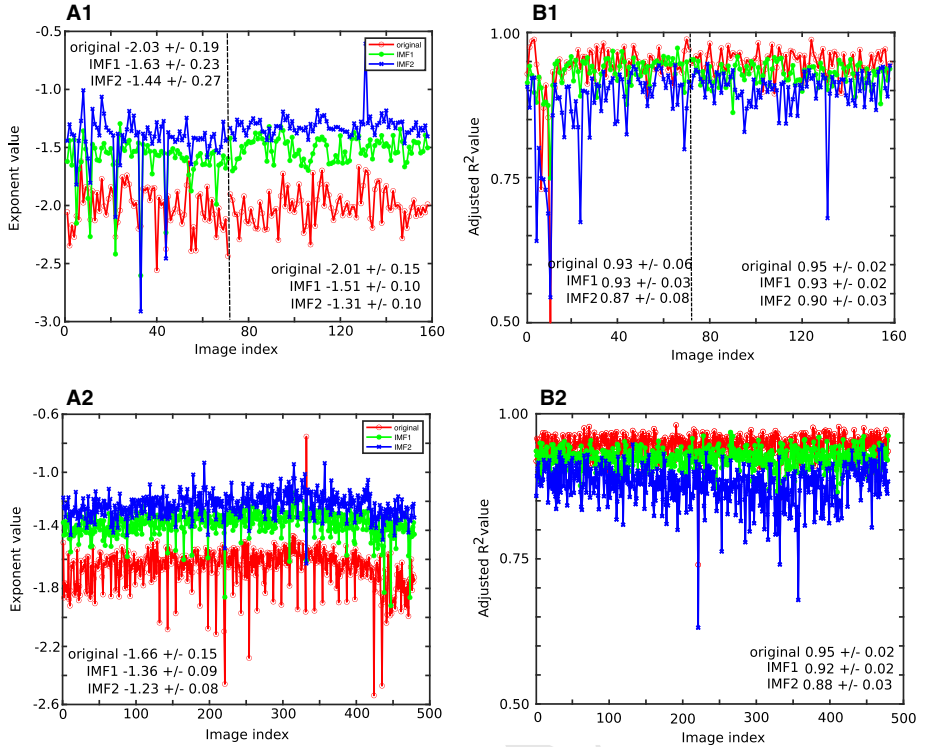


Fig. 5 Power-law exponents and the goodness of fit. Panel A1 (A2) shows the power-law exponents that best fitted the area distributions in the original image (empty red circles), IMF1 (solid green circles), IMF2 (blue “x” marks) for the UP (DOWN) region. The panels B1 and B2 represent the respective goodness of fit measured by the adjusted R^2 value. The mean values (and the standard deviations) of the power-law exponents (panels A1 and A2) decrease in absolute value from the original images to IMF1 and IMF2. The mean value of the adjusted R^2 also decreases from 95 % for the original images to 92 %-93 % for IMF1 and 88 %-90 % for IMF2. All mean values are given with the corresponding standard deviations

Table 1 Power-law exponents extracted from the log-log plot of the area distributions shown in Fig. 4

	original	IMF1	IMF2	IMF3	IMF4
UP window	-2.03 ± 0.19	-1.63 ± 0.23	-1.44 ± 0.27	-1.51 ± 0.29	-1.49 ± 0.29
UP center	-2.01 ± 0.15	-1.51 ± 0.10	-1.31 ± 0.10	-1.36 ± 0.05	-1.35 ± 0.05
DOWN	-1.66 ± 0.15	-1.36 ± 0.09	-1.23 ± 0.08	-1.26 ± 0.07	-1.25 ± 0.07

235 Despite large variabilities and some obvious outliers in the power-law fitting exponents
236 shown in Fig. 4A4-B4, the trends are quite stable. We notice first that the mean values and
237 standard deviations for the first 71 images of the UP region recorded with the focal plane on
238 the sapphire window are within the standard deviation of the next set of images recorded with
239 the focal plane at the center of the SCU (see Table 1). This result has two consequences: 1)
240 supports the ergodic hypothesis that fluctuations have the same structure regardless the focal
241 plane of recordings, and 2) allows us to lump together the first 71 images recorded with the
242 focal plane on the sapphire window with the rest of the UP images recorded with the focal
243 plane at the center of the SCU.

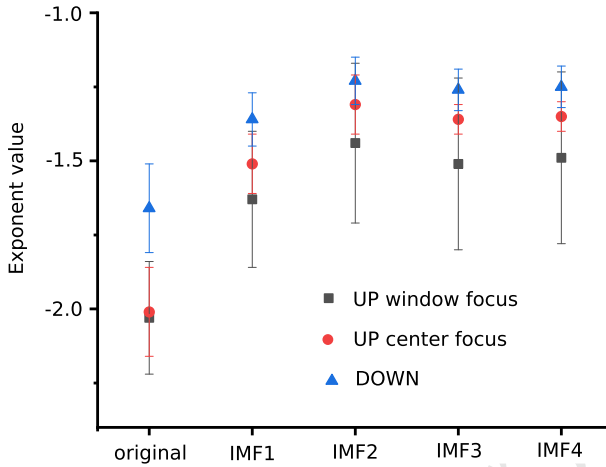


Fig. 6 Mean and standard deviation plots of the power-law exponents for array distributions shown in Fig. 4. The original images gave the largest (in absolute value) exponents with a steady decrease (in absolute value) for IMF1 and IMF2. The exponents for IMF3 and IMF4 are statistically similar, although the actual images are significantly different (see Fig. 1D for IMF3 and Fig. 1E for IMF4). For the UP region, the exponents obtained with the microscope focused on the sapphire window (solid black squares) are statistically identical to those for the microscope focused at the center of the cell (solid red circles). For the DOWN region, the exponents are significantly smaller (in absolute value) compared to UP region (see solid blue triangles)

244 The average exponents that summarize Fig. 4 are given in Table 1 and the corresponding
 245 Fig. 6. As expected, the distribution of areas in the original images (Fig. 4A1-B1) has
 246 the smoothest decay and the largest (absolute value) exponent in Table 1 because they contain
 247 all IMFs.

248 The fact that the exponents for the original images and the first two IMFs are statisti-
 249 cally different suggests that the smoothness of quantitative measures associated with original
 250 images could be misleading because it lumps together processes on different spatial and tem-
 251 poral scales. The similar values of the exponents for IMF3 and IMF4 suggest that, although the
 252 actual images look different, the area measure is not sensitive enough to distinguish between
 253 these two IMFs. This is because both IMF3 and IMF4 contain the largest spatial scales of the
 254 original images, and they do not contain significantly different small-scale convex objects to
 255 tilt the array distribution toward one of the two IMFs.

256 Since the original images include convex objects across all spatial scales, they will be
 257 separated and smoothed by the BEMD image processing when computing IMF1. As a
 258 result, the power-law exponents for IMF1 will reflect the smoothing effect of the BEMD
 259 algorithm leading to a smaller (in absolute value) exponent compared to the original image.
 260 This is because BEMD smoothing of fast spatial oscillations in the original images will
 261 spread the spatial scale over a wider range of sizes. A similar explanation is valid for IMF2.
 262 The saturation and plateau observed for the exponents across IMF2, IMF3, and IMF4 (see
 263 Fig. 6) suggests that we may not have more than two spatial and temporal scales present
 264 in our original image. As a result, adding higher-order IMFs does not add significant new
 265 information to our analysis. Therefore, in the subsequent statistical analysis, we will drop
 266 the last IMF4 as it does not add significantly more information than IMF3.

267 The eccentricity of convex objects in analyzed images indicates possible anisotropy
 268 induced by nucleation [66,67], coalescence-induced coalescence [11,46,54], dimple coa-
 269 lesence [11,57], and other processes that lead to phase separation. The eccentricity of the

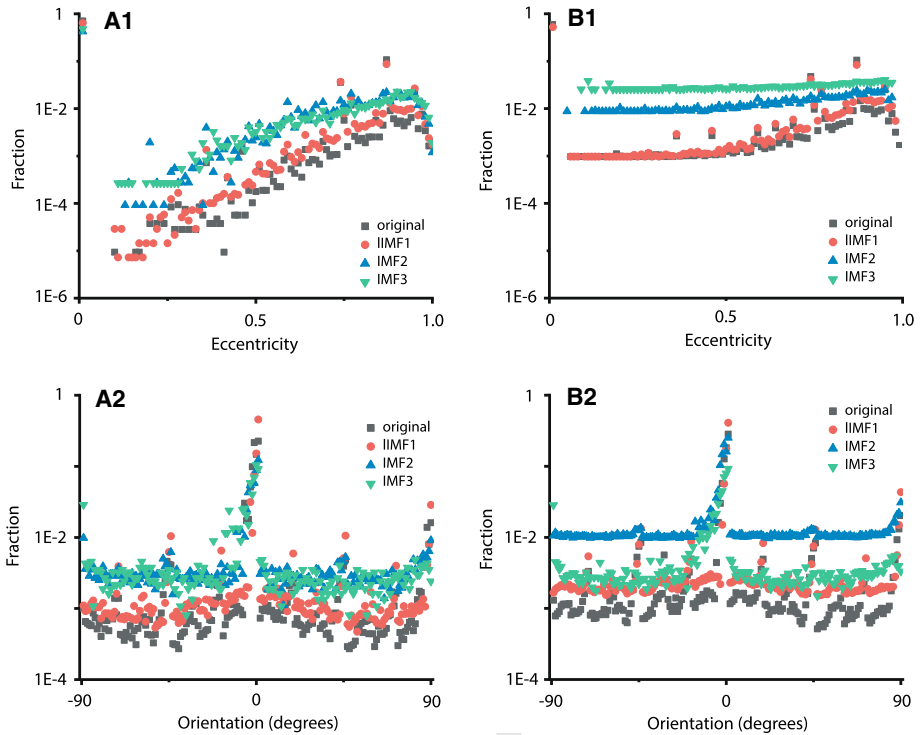


Fig. 7 The eccentricities and orientations of convex areas in fluctuation images. In both UP (left panels A1) and DOWN (right panels B1) regions, the zero-eccentricity (circular cross section) dominates the identified convex objects with larger eccentricities not exceeding 1 % of the total objects identified. The orientations of the elliptical areas are dominated by zero degrees (circles plus some ellipses), and the contribution of other orientations is also less than 1 % (A2 for UP and B2 for DOWN, respectively). All plots are on the semilogarithmic axis to emphasize that nonzero contribution for eccentricity and orientation is tiny

convex objects identified in fluctuation images is measured as the ratio of the distance between the foci of the ellipse and its major axis length (see Fig. 3B). The value of eccentricity is between 0 (circle) and 1 (a line segment). We show the eccentricity on the semilogarithmic axis (see Fig. 7A1 for UP and Fig. 7B1 for DOWN) to emphasize that although objects with nonzero eccentricity were identified in images, their fraction is very small. Indeed, in all original images and the first three IMFs, the largest percentage of objects are circular (no eccentricity), whereas the largest nonzero eccentricity fraction is around 1 %. We summarized in Table 2 the percentage of circular objects identified in the original images and their IMFs. The fact that about 70 % of objects have a circular shape in the UP region aligns with our hypothesis that above the critical point, we only expect short-range correlations that lead to spherical (circular cross section) objects in the absence of any gradients. The fact that over 60 % of objects have a circular shape in the DOWN region indicates that, although the fluctuations are more anisotropic below T_c , the fluid is still very close to T_c in the early stage of phase separation. This suggests that a few tens of μK around T_c , the local field is still pretty uniform, and there is no significant hydrodynamic anisotropy, such as those induced by coalescence-induced coalescence or dimple coalescence [39,56].

Another measure of the system's anisotropy is the orientation of the convex objects in the fluctuation images (see Fig. 3C). We measured the angle between the x-axis and the major axis

Table 2 The percentage of objects with zero eccentricity in Fig. 7A1-B1

	original	IMF1	IMF2	IMF3
UP	71 ± 11	64 ± 13	43 ± 16	48 ± 18
DOWN	60 ± 6	52 ± 6	39 ± 11	45 ± 14

of the elliptical areas identified in fluctuation images, ranging from -90° to 90° . For spherical objects, the algorithm selects the major axis along the x-direction, i.e., 0° orientation. We found that the 0° orientation of convex areas dominates the distribution of orientations. In other words, all zero eccentricity objects (circular cross-section) plus some ellipses that may have 0° orientation (see Fig. 7A2-B2) dominate critical fluctuations very near T_c . We used the semilogarithmic axis again to emphasize that the contribution of orientations other than 0° is below 1%. The very low eccentricity combined with the high ratio of 0° orientation suggests that the fluctuation patterns are relatively homogeneous and mostly spherical very near above and below T_c .

4.2 Spatiotemporal cross sections

The phase separation dynamics that take place near T_c could be captured by the spatiotemporal “waterfalls,” i.e., temporal stacks of single-pixel lines. The morphological properties identified in the previous section only capture a few features of critical fluctuations very near above and below the critical temperature.

We determined the distribution of contiguous black pixels along the horizontal (spatial) direction of “waterfalls” shown in Fig. 2. Such a distribution gives information about the spatial size of fluctuations and is shown in Fig. 8A1-A2. For all microscopic images, the 1 pixel = $3.1 \mu\text{m}$. The “waterfall”’s spatial dimension statistics contain different information than the distribution of the areas of convex objects identified through morphology analysis. In the spatiotemporal images (see Fig. 2), we analyze the evolution of contiguous linear domains at the same location across all original images and their IMFs. While it is possible for a cross section of an image to contain the same information about the statistics of fluctuations as the whole image, such an ergodic assumption is only valid in the limit of a very large cross section. Due to the finite size of the cross section, i.e., a one-pixel line from each image, we expect slightly different power-law exponents for the spatiotemporal cross sections compared to the morphology analysis.

All spatial distributions for all original images and their IMFs have the same general structure: they monotonically increase to a peak and then decay as a power-law (shown as straight-line patterns in a log-log plot of Fig. 8A1-A2). We fitted the spatial distribution data with a power-law over an adjustable range of distances that gave us the best goodness of fit with the maximum possible coefficient of determination. For example, for the original image in Fig. 8A1, the best range was 3 to 24 pixels; for IMF1, the range was 4 to 20 pixels; for IMF2 was 6 to 29 pixels, and for IMF3, it was 14 to 52 pixels.

There are similarities between the spatiotemporal statistics (Table 3) and convex area statistics from morphology analysis (Table 1). In both cases, the power-law exponents increase from the original images as the IMF order increases. Such consistent behavior supports the ergodic hypothesis, i.e., the dynamics of fluctuations is the same whether we analyze the whole image using morphology measures or only a cross section as in the case of “waterfalls.” The second conclusion from the power-law exponents’ consistent trend is that the fractal hypothesis is supported by the existence of power-laws holds across all IMFs. We noticed

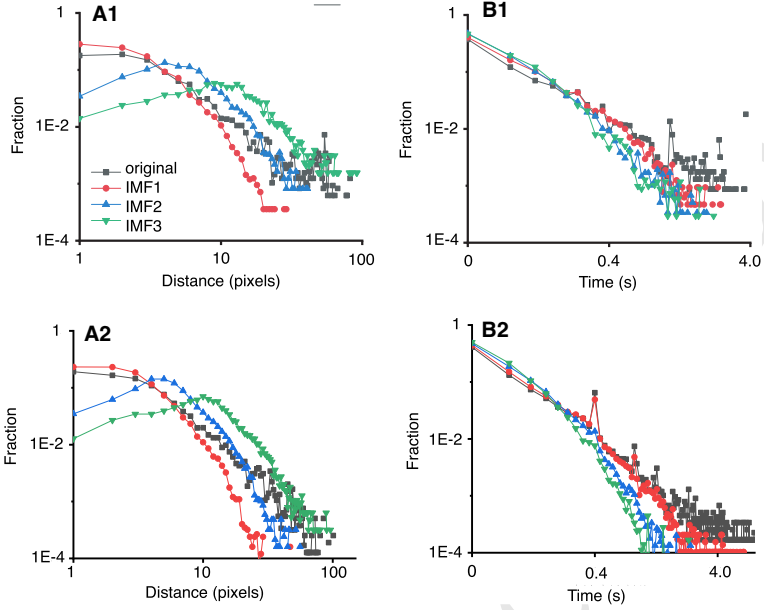


Fig. 8 Distributions of spatial (A1-A2) and temporal (B1-B2) fluctuation sizes. The spatial size of fluctuations has a peak that depends on the IMF's spatial scale (A1 for UP and A2 for DOWN). Spatial unit is 1 pixel = 3.1 μm . After the peak, all distributions decay as power laws with quite close exponents (see Table 4). The distribution of temporal correlations for all IMFs follows identical patterns with two different exponents: a relatively small exponent for durations shorter than 0.4 s and a much more negative exponent for longer correlation times (B1 for UP and B2 for DOWN). There were 25 frames per second

Table 3 The power law exponent of spatial distribution of objects in Fig. 8A1-A2. The distances are measured in pixels with 1 pixel = 3.1 μm

	original	IMF1	IMF2	IMF3
UP	-1.75 ± 0.04	-2.19 ± 0.08	-2.30 ± 0.07	-2.4 ± 0.1
DOWN	-0.93 ± 0.05	-0.94 ± 0.10	-2.50 ± 0.05	-2.45 ± 0.06

328 in both the morphology analysis (Table 1) and the spatiotemporal cross sections (Table 3)
 329 that the exponents of the original images and IMF1 are very close, which suggests that the
 330 critical fluctuations are captured for the most part by the finest spatial scale of IMF1.

331 There are also differences between UP and DOWN plateaus revealed by spatial statistics.
 332 For example, the power-law exponents of spatiotemporal cross sections for both the original
 333 and IMF1 in the UP region are about twice as large as the exponents for the DOWN region
 334 (Table 3). This shows that, although the fractal nature of fluctuations revealed by the power-
 335 laws is preserved, the DOWN region has a much smoother distribution of linear sizes. Another
 336 significant difference is that the power-law exponent increases from the original image to
 337 IMF1 only for the UP region (Table 1 and Table 3), whereas for DOWN, the exponents are
 338 almost constant. This means that below T_c , both the original and IMF1 have similar spatial
 339 dynamics.

340 The distribution of temporal correlations measured along the temporal axis (vertical)
 341 direction has completely different dynamics than the spatial correlation, as shown in Fig. 8B1-

Table 4 The power-law exponent of temporal distribution from Fig. 8B1-B2

	original	IMF1	IMF2	IMF3
UP ($t < 0.4$ s)	-1.44 ± 0.04	-1.48 ± 0.02	-1.32 ± 0.03	-1.41 ± 0.08
UP ($t > 0.4$ s)	-1.6 ± 0.1	-2.5 ± 0.3	-3.2 ± 0.4	-2.4 ± 0.3
DOWN ($t < 0.4$ s)	-1.42 ± 0.03	-1.39 ± 0.03	-1.33 ± 0.04	-1.39 ± 0.06
DOWN ($t > 0.4$ s)	-1.7 ± 0.12	-2.26 ± 0.10	-3.5 ± 0.2	-3.0 ± 0.4

342 B2. All IMFs have almost the same power-law distribution up to 0.4 s (the equivalent of 10
343 video frames), and then the power-law exponent drops significantly (see Fig. 8B1-B2 and
344 Table 4). The fact that there are two different exponents for the temporal correlation suggests
345 that indeed the correlation time of fluctuations is best described by a double exponential
346 [39,55,56]. The difference in the two exponents is clear when comparing the fitting for short
347 durations $t < 0.4$ s against longer durations with $t > 0.4$ s for all IMFs (see Fig. 8B1-B2
348 and Table 4). The temporal correlation exponent (Table 4) for short durations (below 0.4 s) is
349 statistically identical both for the UP and the DOWN regions. Moreover, the exponents are
350 almost constant across the original images and their IMFs. This suggests that fluctuations in
351 the temporal statistics are not sensitive to spatial scale separation performed with the BEMD.
352 The characteristic times of fluctuations decrease as $t^{-1.4}$ for the original images.

353 For longer correlation times (above 0.4 s), the distribution scales as $t^{-1.7}$ and is no longer
354 invariant to BEMD spatial decomposition. The increase in the power-law exponents with the
355 IMF order indicates that larger fluctuations lose temporal correlation much faster than smaller
356 clusters. As expected, the original image's power-law exponents do not show such a large
357 discontinuity because it lumps together multiple spatial and temporal scales (see Table 4).
358 For this reason, in the DDM analysis of fluctuation images the correlation time of fluctuations
359 is represented by a single power-law exponent [3, 19–21, 33, 61, 75, 76].

360 5 Conclusions

361 The recent extension of the classical theory of fluctuations to non-equilibrium processes
362 [76] showed that the temporal correlation of fluctuations could be directly obtained from
363 fluctuation images. It can lead to experimental advances in measuring diffusion and viscosity
364 coefficients. The information regarding the evolution and the scaling of the fluctuation
365 correlation time is contained in the Intermediate Scattering Function (ISF). For pure fluid
366 in thermal equilibrium, the ISF is a Gaussian with width proportional to the diffusion time.
367 There are cases when ISF contains multiple time scales, and one approach for mitigating
368 this issue has been the fitting of ISF with multiple exponentials to capture each characteristic
369 time separately [3,61]. This approach allowed, for example, the separation of the thermal
370 diffusivity coefficient from the mass diffusivity [3].

371 Instead of investigating the fluctuations in Fourier space through their ISFs, we here carried
372 out a direct space analysis of fluctuations. For this purpose, we used the BEMD, data-driven
373 technique to decompose the spatial frequency components into an orthogonal set of Intrinsic
374 Mode Function (IMFs). This method is suitable for analyzing nonlinear and non-stationary
375 data, such as the thermal quench data that stepped through the critical temperature T_c in our
376 microgravity experiment.

377 Different physical processes act over different spatial and temporal ranges. Very near the
378 critical point of a phase transition, dynamical fluctuations reach macroscopic magnitude and
379 overrule molecular size, shape, and interactions in dictating bulk behavior [22,78]. These
380 fluctuations are generated by the nonlinear dynamics of classical critical fluids. Recent large-
381 scale numerical simulations showed that when approaching the liquid-vapor critical point
382 from the supercritical regime, $T > T_c$, the Lyapunov exponents associated with the phase
383 space dynamics of molecules decrease monotonically [22]. This is due to the fact that critical
384 fluctuations imply structural organization as opposed to molecular chaos and dynamic
385 instability. The Lyapunov exponents measure how quickly infinitesimally closed phase space
386 points separate over time. Large Lyapunov exponents indicate more unstable phases space
387 dynamics. As the system approaches T_c from above, the divergence of trajectories “slows
388 down” and allows the formation of spatial regions in the system that will separate into coex-
389 isting vapor and liquid phases below T_c .

390 We found consistent power-laws across all spatial scales, which supports our hypothesis
391 of critical fluctuations’ fractal nature. The morphology analysis showed that very near T_c , the
392 fluctuating domains are mostly spherical with some anisotropy. Spatiotemporal cross sections
393 showed that the distribution of contiguous domains also obeys free-scale power-laws near
394 T_c that support the fractal hypothesis of critical fluctuations. The temporal correlation of
395 fluctuations also follows a power-law with the same exponent across all spatial scales (for
396 correlation times shorter than 0.4s (10 video frames). This surprising result supports the
397 hypothesis of a “slowing down” in the divergence of molecular trajectories [22] across all
398 spatial scales to allow phase separation.

399 **Acknowledgements** AO and SAO acknowledge 2020-2021 Mini-Research and Education Awards Program
400 and Palmetto Academy grants from South Carolina Space Grant/EPSCoR in support for this research. SAO
401 acknowledges a 2020-2021 Research and Development grant from the College of Charleston. YG, CL and
402 DB. acknowledge a research grant from Centre National d’Études Spatiales (CNES) and a NASA grants
403 NAG3-1906 and NAG3-2447.

404 **Author contributions** AO and SAO perform image and statistical analysis. YG, CL, and DB conducted the
405 microgravity experiments and contributed to data analysis. All authors wrote the paper together and approved
406 the final manuscript.

407 References

- 408 1. P.F. Alvanitopoulos, A. Moroi, G. Bagropoulos, K. Dundon, Content Based Image Retrieval and Its
409 Application to Product Recognition, in *Artificial Intelligence Applications and Innovations*. ed. by R.
410 Chbeir, Y. Manolopoulos, I. Maglogiannis, R. Alhadj. pp. (Springer International Publishing, Cham,
411 2015), pp. 3–18
- 412 2. W. Asher, J.F. Pankow, Direct observation of concentration fluctuations close to a gas-liquid interface.
413 *Chem. Eng. Sci.* **44**(6), 1451–1455 (1989)
- 414 3. H. Bataller, C. Giraudet, F. Croccolo, and J. Maria Ortiz de Zarate. Analysis of Non-Equilibrium Fluctu-
415 ations in a Ternary Liquid Mixture. *Microgravity Science and Technology*, 28, 2016
- 416 4. F. Ben Arfia, A. Sabri, M. Ben Messaoud, and M. Abid. The bidimensional empirical mode decomposition
417 with 2D-DWT for gaussian image denoising. In *2011 17th International Conference on Digital Signal
418 Processing (DSP)*, pages 1–5, 2011
- 419 5. Bertrand Berche, Malte Henkel, and Ralph Kenna. Critical phenomena: 150 years since cagniard de la
420 tour. *Revista Brasileira de Ensino de Física*, 31:2602.1 – 2602.4, 06 2009
- 421 6. B.J. Berne, R. Pecora. *Dynamic Light Scattering: With Applications to Chemistry, Biology, and Physics
422 Dover Books on Physics Series* (Dover Publications, New York, 2000)
- 423 7. D. Beysens. Critical Phenomena. *Materials Sciences in Space, a Contribution to the Scientific Basis of
424 Space Processing*, page 191, 1986

- 425 8. D. Beysens, D. Estève, Adsorption phenomena at the surface of silica spheres in a binary liquid mixture.
426 Phys. Rev. Lett. **54**, 2123–2126 (1985)
- 427 9. D. Beysens, M. Gbadamassi, L. Boyer, Light-scattering study of a critical mixture with shear flow. Phys.
428 Rev. Lett. **43**, 1253–1256 (1979)
- 429 10. D. Beysens, P. Guenoun, and F. Perrot. Direct observation of critical fluctuations. *Journal of Physics:*
430 *Condensed Matter*, 2:SA127–SA133, 1990
- 431 11. A. Daniel, Beysens, Kinetics and morphology of phase separation in fluids: The role of droplet coalescence.
432 Phys. A: Stat Mech Appl **239**(1), 329–339 (1997)
- 433 12. Juan Camilo Bohorquez, Sean Gourley, Alexander R. Dixon, Michael Spagat, and Neil F. Johnson.
434 Common ecology quantifies human insurgency. *Nature*, 462:911–914, 2009
- 435 13. J.M. Carlson, J.S. Langer, Mechanical model of an earthquake fault. Phys. Rev. A **40**, 6470–6484 (1989)
- 436 14. R. Cerbino, A. Vailati, Near-field scattering techniques: Novel instrumentation and results from time and
437 spatially resolved investigations of soft matter systems. *Curr. Opin Coll Interface Sci.* **14**(6), 416–425
438 (2009)
- 439 15. L. Chen, *Handbook of Research on Advancements in Supercritical Fluids Applications for Sustainable*
440 *Energy Systems Advances in Chemical and Materials Engineering* (IGI Global, Hershey, 2020)
- 441 16. Y.Q. Chen, L.N. Zhang, B.B. Zhao, Application of Bi-dimensional empirical mode decomposition
442 (BEMD) modeling for extracting gravity anomaly indicating the ore-controlling geological architec-
443 tures and granites in the gejiu tin-copper polymetallic ore field, southwestern china. *Ore Geol. Rev.* **88**,
444 832–840 (2017)
- 445 17. Aaron Clauset, Cosma Rohilla Shalizi, and M. E. J. Newman. Power-law distributions in empirical data.
446 *SIAM Review*, 51(4):661-703, Nov 2009
- 447 18. Antonio Coniglio. Percolation and critical points. *Journal of Physics: Condensed Matter*, 13(41):9039–
448 9053, sep 2001
- 449 19. F. Crocco. *Dynamics of Non Equilibrium Fluctuations in Free Diffusion*. Thesis, 2006
- 450 20. F. Crocco, D. Brogioli, A. Vailati, M. Giglio, D.S. Cannell, Use of dynamic schlieren interferometry to
451 study fluctuations during free diffusion. *Appl. Opt.* **45**(10), 2166–2173 (2006)
- 452 21. F. Crocco, C. Giraudet, H. Battaler, R. Cerbino, A. Vailati, Shadowgraph analysis of non-equilibrium
453 fluctuations for measuring transport properties in microgravity in the GRADFLEX experiment. *Micro-*
454 *gravity Sci. Technol.* **28**(4), 467–475 (2016)
- 455 22. M. Das, J.R. Green, Critical fluctuations and slowing down of chaos. *Nat. Commun.* **10**, 2155 (2019)
- 456 23. P. Debye, R.T. Jacobsen, Direct visual observation of concentration fluctuations in a critical mixture. *J.*
457 *Chem. Phys.* **48**(1), 203–206 (1968)
- 458 24. L.A. Dissado, R.M. Hill, Self-similarity as a fundamental feature of the regression of fluctuations. *Chem.*
459 *Phys.* **111**(2), 193–207 (1987)
- 460 25. C. Domb, Critical phenomena: a brief historical survey. *Contemporary Phys.* **26**(1), 49–72 (1985)
- 461 26. C. Domb, *The Critical Point: A Historical Introduction to the Modern Theory of Critical Phenomena*
462 (CRC Press, Florida, 1996)
- 463 27. W. Dong, X. Li, X. Lin, and Z. Li. A Bidimensional Empirical Mode Decomposition Method for Fusion of
464 Multispectral and Panchromatic Remote Sensing Images. *Remote Sensing*, 6:8446–8467, 09 2014
- 465 28. Alain Durieux and Isabelle Petitbon. ALICE: optical instrument for observation, interferometry, and
466 diffusion of critical fluids in microgravity. In Thierry M. Dewandre, Joachim J. Schulte in-den Baeumen,
467 and Emmanuel Sein, editors, *Space Optics 1994: Space Instrumentation and Spacecraft Optics*, volume
468 2210, pages 249 – 258. International Society for Optics and Photonics, SPIE, 1994
- 469 29. E. Michael, Fisher, Helen Au-Yang, Critical wall perturbations and a local free energy functional. *Phys.*
470 *A: Stat. Mech. Appl.* **101**(1), 255–264 (1980)
- 471 30. Michael E. Fisher, Michael N. Barber, Scaling theory for finite-size effects in the critical region. *Phys.*
472 *Rev. Lett.* **28**, 1516–1519 (1972)
- 473 31. A. Garcia-Perez, J.P. Amezquita-Sanchez, A. Dominguez-Gonzalez, R. Sedaghati, R. Osornio-Rios, R.J.
474 Romero-Troncoso, Fused empirical mode decomposition and wavelets for locating combined damage in
475 a truss-type structure through vibration analysis. *J. Zhejiang Univ. Science A* **14**(9), 615–630 (2013)
- 476 32. F. Giavazzi, D. Brogioli, V. Trappe, T. Bellini, R. Cerbino, Scattering information obtained by optical
477 microscopy: Differential dynamic microscopy and beyond. *Phys. Rev. E* **80**, 031403 (2009)
- 478 33. F. Giavazzi, A. Fornasieri, A. Vailati, R. Cerbino, Equilibrium and non-equilibrium concentration fluctu-
479 ations in a critical binary mixture. *Europ. Phys. J. E* **39**(10), 103 (2016)
- 480 34. L. Guang, L. Li, H. Gong, Q. Jin, X. Li, R. Song, Y. Chen, Y. Chen, C. He, Y. Huang, Y. Yao, Multisource
481 remote sensing imagery fusion scheme based on bidimensional empirical mode decomposition (BEMD)
482 and its application to the extraction of bamboo forest. *Remote Sens.* **9**, 19 (2016)
- 483 35. P. Guenoun, R. Gastaud, F. Perrot, D. Beysens, Spinodal decomposition patterns in an isodensity critical
484 binary fluid: Direct-visualization and light-scattering analyses. *Phys. Rev. A* **36**(10), 4876 (1987)

- 485 36. P. Guenoun, F. Perrot, D. Beysens, Microscopic observation of order-parameter fluctuations in critical
486 binary fluids: Morphology, self-similarity, and fractal dimension. *Phys. Rev. Lett.* **63**(11), 1152 (1989)
- 487 37. Z. He, Q. Wang, Y. Shen, J. Jin, Y. Wang, Multivariate gray model-based bemd for hyperspectral image
488 classification. *IEEE Trans. Instrum. Measure.* **62**(5), 889–904 (2013)
- 489 38. J. Hegseth, A. Oprisan, Y. Garrabos, V.S. Nikolayev, C. Lecoutre-Chabot, D. Beysens, Wetting film
490 dynamics during evaporation under weightlessness in a near-critical fluid. *Phys. Rev. E* **72**(3), 031602
491 (2005)
- 492 39. J.J. Hegseth, A. Oprisan, Y. Garrabos, D. Beysens, Imaging critical fluctuations of pure fluids and binary
493 mixtures. *Phys. Rev. E* **90**, 022127 (2014)
- 494 40. J. Huang, B. Zhao, Y. Chen, P. Zhao, Bidimensional empirical mode decomposition (BEMD) for extraction
495 of gravity anomalies associated with gold mineralization in the tongshi gold field, western shandong
496 uplifted block, eastern china. *Comput. Geosci.* **36**(7), 987–995 (2010)
- 497 41. J.-Y. Huang, K.-L. Wen, X.-J. Li, J.-J. Xie, C.-T. Chen, S.-C. Su, Coseismic deformation time history
498 calculated from acceleration records using an EMD-derived baseline correction scheme: a new approach
499 validated for the 2011 Tohoku Earthquake. *Bull. Seismol. Soc. Am.* **103**(2B), 1321–1335 (2013)
- 500 42. N.E. Huang, Z. Shen, S.R. Long, M.C. Wu, H.H. Shih, Q. Zheng, N-C Yen, C.C. Tung, and H.H. Liu.
501 The empirical mode decomposition and the hilbert spectrum for nonlinear and non-stationary time series
502 analysis. *Proceedings of the Royal Society of London. Series A: Mathematical, Physical and Engineering
503 Sciences*, 454(1971):903–995, 1998
- 504 43. S. Huang, Z. Liu, Z. Liu, L. Wang, Sar image change detection algorithm based on different empirical
505 mode decomposition. *J. Comput. Commun.* **5**, 9–20 (2017)
- 506 44. W. Huang, Z. Shen, N.E. Huang, Y.C. Fung, Use of intrinsic modes in biology: Examples of indicial
507 response of pulmonary blood pressure to step hypoxia. *Procee. Nat. Academy Sci.* **95**(22), 12766–12771
508 (1998)
- 509 45. C.N. Jean, Y. Bouaoune, D. Eric, N. Oumar, P. Bunel, Image analysis by bidimensional empirical mode
510 decomposition. *Image Vision Comput.* **21**, 1019–1026 (2003)
- 511 46. Tomasz Kalwarczyk, Natalia Ziebaczk, Marcin Fialkowski, Robert Holyst, Late stage of the phase-
512 separation process: Coalescence-induced coalescence, gravitational sedimentation, and collective evap-
513 oration mechanisms. *Langmuir* **24**(13), 6433–6440 (2008)
- 514 47. M. Kikuchi, Y. Okabe, A scaling approach to monte carlo renormalization group. *Prog. Theo. Phys.* **78**(3),
515 540–551 (1987)
- 516 48. Tiina Komulainen. Self-similarity and power laws. Technical report, Helsinki University of Technology,
517 2004
- 518 49. J.-M. Laherrère and P. Koutsikides. Alice, an instrument for the analysis of fluids close to the critical
519 point in microgravity. *Acta Astronautica*, 29(10):861–870, 1993. World Space Congress
- 520 50. D. Liu, X. Chen, Image denoising based on improved bidimensional empirical mode decomposition
521 thresholding technology. *Multimedia Tools Appl.* **78**, 7381–7417 (2018)
- 522 51. R. Marcout, J.F. Zwillling, J.M. Laherrere, Y. Garrabos, and Beysens D. ALICE 2, an advanced facility
523 for the analysis of fluids close to their critical point in microgravity. In *45th Congress of the International
524 Astronautical Federation, Jerusalem, Israel*. International Astronautical Federation, 1994
- 525 52. A. Moreno-Gomez, J.P. Amezquita-Sanchez, M. Valtierra-Rodriguez, C.A. Perez-Ramirez, A.
526 Dominguez-Gonzalez, O. Chavez-Alegria, Emd-shannon entropy-based methodology to detect incipient
527 damages in a truss structure. *Appl. Sci.* **8**(11), 2068 (2018)
- 528 53. J. Oh, J.M. Ortiz de Zárate, J.V. Sengers, G. Ahlers, Dynamics of fluctuations in a fluid below the onset
529 of Rayleigh-Bénard convection. *Phys. Rev. E* **69**, 021106 (2004)
- 530 54. A. Oprisan, C. Garrabos, Y. Lecouter, D. Beysens, Measuring the transition rates of coalescence events
531 during double phase separation in microgravity. *Molecules* **22**, 1125 (2017)
- 532 55. A. Oprisan, S.A. Oprisan, J.J. Hegseth, Y. Garrabos, C. Lecoutre-Chabot, D. Beysens, Universality in
533 early-stage growth of phase-separating domains near the critical point. *Phys. Rev. E* **77**(5 Pt 1), 051118
534 (2008)
- 535 56. A. Oprisan, S.A. Oprisan, B. Bayley, J.J. Hegseth, Y. Garrabos, C. Lecoutre-Chabot, D. Beysens, Dynamic
536 structure factor of density fluctuations from direct imaging very near (both above and below) the critical
537 point of SF₆. *Phys. Rev. E* **86**, 061501 (2012)
- 538 57. A. Oprisan, S.A. Oprisan, J.J. Hegseth, C. Garrabos, Y. Lecouter, D. Beysens, Dimple coalescence and
539 liquid droplets distributions during phase separation in a pure fluid under microgravity. *Eur. Phys. J. E*
540 **37**, 1–10 (2014)
- 541 58. A. Oprisan, S.A. Oprisan, J.J. Hegseth, C. Garrabos, Y. Lecouter, D. Beysens, Direct imaging of long-range
542 concentration fluctuations in a ternary mixture. *Eur. Phys. J. E* **38**, 1–9 (2015)
- 543 59. Ana Oprisan, Brittany Bayley, Sorinel A. Oprisan, John J. Hegseth, Yves Garrabos, Carole Lecoutre, and
544 Daniel Beysens. Thermal fluctuation exponents for two near-critical point systems. In Zia ur Rahman,

- 545 Stephen E. Reichenbach, and Mark A. Neifeld, editors, *Visual Information Processing XIX*, volume 7701,
546 pages 220 – 229. International Society for Optics and Photonics, SPIE, 2010
- 547 60. Ana Oprisan, Yves Garrabos, Carole Lecoutre-Chabot, Daniel Beysens, Multiscale empirical mode
548 decomposition of density fluctuation images very near above and below the critical point of sf6. *Physica*
549 *A: Stat. Mech. Appl.* **561**, 125293 (2021)
- 550 61. J.M. Ortiz de Zarate, C. Giraudet, H. Bataller, and F. Croccolo. Non-equilibrium fluctuations induced by
551 the Soret effect in a ternary mixture. *The European Physical Journal E: Soft Matter*, 37:34, 08 2014
- 552 62. N. Otsu, A threshold selection method from gray-level histograms. *IEEE Trans. Syst. Man Cybern.* **9**(1),
553 62–66 (1979)
- 554 63. V. Pareto. *Cours d'Economie Politique Professe a l'Universite de Lausanne*. F. Rouge, 1897
- 555 64. S.T.G. Raghukanth, S. Sangeetha, Empirical mode decomposition of earthquake accelerograms. *Adv.*
556 *Adapt. Data Anal.* **04**(04), 1250022 (2012)
- 557 65. G. Rilling, P. Flandrin, P. Goncalves, J.M. Lilly, Bivariate empirical mode decomposition. *IEEE Signal*
558 *Process. Lett.* **14**(12), 936–939 (2007)
- 559 66. C. Sagui, M. Grant, Theory of nucleation and growth during phase separation. *Phys. Rev. E* **59**(4), 4175
560 (1999)
- 561 67. C. Sagui, D.S. O’Gorman, M. Grant, Nucleation, growth and coarsening in phase-separating systems.
562 *Scan. Microsc.* **12**(1), 3–8 (1998)
- 563 68. A. Saha, M. Pukhrabam, S.N. Pradhan, Facial image analysis for expression recognition by bidimen-
564 sional empirical mode decomposition. *Indian J. Sci. Technol.* **9**(31), 1–9 (2016)
- 565 69. N.A. Salingaros, B.J. West, A universal rule for the distribution of sizes. *Environ. Plan. B: Plan. Design*
566 **26**(6), 909–923 (1999)
- 567 70. Helmut Satz, Cluster percolation and thermal critical behavior. *Comput. Phys. Commun.* **147**(1), 46–51
568 (2002)
- 569 71. R.E. Seoud, J.C. Vassilicos, Dissipation and decay of fractal-generated turbulence. *Phys. Fluids* **19**(10),
570 105108 (2007)
- 571 72. H. Song, H. Bai, L. Pinheiro, C. Dong, C.-Y. Huang, B. Liu, Analysis of ocean internal waves imaged
572 by multichannel reflection seismics, using ensemble empirical mode decomposition. *J. Geophys. Eng.* **9**,
573 302–311 (2012)
- 574 73. Masuo Suzuki. Static and Dynamic Finite-Size Scaling Theory Based on the Renormalization Group
575 Approach. *Progress of Theoretical Physics*, 58(4):1142–1150, 10 1977
- 576 74. Masuo Suzuki. Phase Transition and Fractals. *Progress of Theoretical Physics*, 69(1):65–76, 01 1983
- 577 75. A. Vailati, R. Cerbino, S. Mazzoni, C.J. Takacs, D.S. Cannell, M. Giglio, Fractal fronts of diffusion in
578 microgravity. *Nat. Commun.* **2**(290), 1–5 (2011)
- 579 76. A. Vailati, M. Giglio, Nonequilibrium fluctuations in time-dependent diffusion processes. *Phys. Rev. E*
580 **58**, 4361–4371 (1998)
- 581 77. Alberto Vailati, Marzio Giglio, Giant fluctuations in a free diffusion process. *Nature* **390**(6657), 262–265
582 (1997)
- 583 78. B. Widom, Intermolecular forces and the nature of the liquid state. *Science* **157**(3787), 375–382 (1967)
- 584 79. S. Will, A. Leipertz, Mutual diffusion coefficient and dynamic viscosity near the critical consolute point
585 probed by dynamic light scattering. *Int. J. Thermophys.* **20**(3), 791–803 (1999)
- 586 80. Kenneth G. Wilson. Renormalization group and critical phenomena. i. renormalization group and the
587 kadanoff scaling picture. *Phys. Rev. B*, 4:3174–3183, Nov 1971
- 588 81. Kenneth G. Wilson and Michael E. Fisher. Critical exponents in 3.99 dimensions. *Phys. Rev. Lett.*, 28:240–
589 243, Jan 1972
- 590 82. Y. Xu, B. Liu, J. Liu, S. Riemenschneider, Two-dimensional empirical mode decomposition by finite
591 elements. *Procee. Royal Soc. A: Math. Phys. Eng. Sci.* **462**(2074), 3081–3096 (2006)
- 592 83. Shunsuke Yabunaka, Akira Onuki, Critical adsorption profiles around a sphere and a cylinder in a fluid
593 at criticality: Local functional theory. *Phys. Rev. E* **96**, 032127 (2017)
- 594 84. J. Zheng, J. Cheng, Y. Yang, Generalized empirical mode decomposition and its applications to rolling
595 element bearing fault diagnosis. *Mech. Syst. Signal Process.* **40**(1), 136–153 (2013)
- 596 85. J. Zheng, H. Pan, S. Yang, J. Cheng, Generalized composite multiscale permutation entropy and laplacian
597 score based rolling bearing fault diagnosis. *Mech. Syst. Signal Process.* **99**, 229–243 (2018)